


Article

Bistatic-ISAR Linear Geometry Distortion Alleviation of Space Targets

Lin Shi ¹ , Baofeng Guo ^{1,*}, Ning Han ^{2,*}, Juntao Ma ¹, Xiaoxiu Zhu ¹ and Chaoxuan Shang ¹

¹ Department of Electronic and Optical Engineering, Army Engineering University Shijiazhuang Campus, Shijiazhuang 050003, China; shilin85@foxmail.com (L.S.); tm2001@sina.com (J.M.); zhuxiaoxiu13@163.com (X.Z.); scx1207@sina.com (C.S.)

² PLA 32181 Unit, Shijiazhuang 050003, China

* Correspondence: guobao_feng870714@126.com (B.G.); haning1103@163.com (N.H.); Tel.: +86-031-187-994245 (B.G.); +86-031-181-563176 (N.H.)

Received: 28 March 2019; Accepted: 16 May 2019; Published: 20 May 2019



Abstract: The linear geometry distortion caused by time variant bistatic angles induces the sheared shape of the bistatic inverse synthetic aperture radar (bistatic-ISAR) image. A linear geometry distortion alleviation algorithm for space targets in bistatic-ISAR systems is presented by exploiting prior information. First, we analyze formation mathematics of linear geometry distortions in the Range Doppler (RD) domain. Second, we estimate coefficients of first-order polynomial of bistatic angles by least square error (LSE) method through exploiting the imaging geometry and orbital information of space targets. Third, we compensate the linear spatial-variant terms to restore the linear geometry distortions. Consequently, the restored bistatic-ISAR image with real shape is obtained. Simulated results of the ideal point scatterers dataset and electromagnetic numerical dataset verify the performance of the proposed algorithm.

Keywords: bistatic inverse synthetic aperture radar; linear geometry distortion; prior information; least square error

1. Introduction

The monostatic inverse synthetic aperture radar (ISAR) system provides electromagnetic images of targets in the Range Doppler (RD) domain [1–4], which is suitable for the target recognition [5]. However, in monostatic ISAR systems, the image cannot be obtained when targets only move along the line of sight (LOS) of radar within the coherent process interval (CPI). To overcome this limitation, the bistatic configuration is introduced for the ISAR system [6]. In bistatic radar systems, the transmitting station and receiving station are separated spatially, and the length of the baseline is comparable to the distance of targets. The bistatic configuration is capable of obtaining complementary information of the target and providing better anti-jamming ability [6]. Hence, the bistatic-ISAR system has been an effective solution for space targets surveillance [7–12]. The bistatic-ISAR research, with respect to application and algorithm, has been studied in recent years [6,13–19].

Synchronization issues between the transmitting station and receiving station are inherent for the practical bistatic-ISAR configuration. Both the back-projection (BP) algorithm [20] and the polar-format-algorithm (PFA) [21] are sensitive to synchronization accuracy. Thus, applicability of those two algorithms is limited in bistatic-ISAR systems [13]. The RD imaging algorithm, with low requirement for synchronization accuracy and concise physical meaning, is widely used for simulated and real data process in bistatic-ISAR systems [6,8,14]. The bistatic equivalent monostatic (BEM) radar, an approximation of bistatic-ISAR systems, is derived, subject to certain constraints [14]. It effectively simplifies the bistatic-ISAR signal processing. The bistatic angle is the angle between the LOS of the

transmitting station and receiving station. The time variant bistatic angles are caused by the bistatic configuration. However, the linear geometry/quadratic-defocusing distortions are caused by time variant bistatic angles when using the RD imaging algorithm [6,13,22].

In [16], a distortions mitigation algorithm based on “linked scatterers” to alleviate the distortions are introduced. However, this algorithm requires the transmitting station to work in duplex mode. Recently, a distortions mitigation algorithm was proposed in [22] by combining CPI reduction with super-resolution algorithms. However, the reduction factor of CPI needs to be deliberately calculated to guarantee that the distortions are less than corresponding resolution. Moreover, the tradeoff between distortion alleviation and resolution is required, even if using super resolution algorithms. In other words, higher resolution can be achieved in the same case, if the alleviation can be completed without reduction of CPI. Furthermore, the problem induced by the linear geometry distortion is more serious than the quadratic-defocusing one [23] in generic bistatic-ISAR systems. The linear geometry distortion causes a sheared target shape, since the linear Doppler shift of scatters in different range-bins change with the range position. It is almost impossible to perform target recognition with the sheared shape image. To alleviate the linear geometry distortions, the interferometric technique is adopted in bistatic-ISAR systems [24]. However, a super-receiver with at least three antennas needs to be configured for the interferometric technique. Both structure and complexity of the system are increased fast with an increasing antenna number, as compared with the classical bistatic-ISAR system with one transmitting station and one receiving station. Conversely, linear geometry distortion alleviation algorithms by exploiting prior information are promising solutions. In [25] we estimate the image distortion angle for space targets by exploiting prior information. By calculating the image distortion angle that we defined in [26], the linear geometry distortion alleviation is conducted in each range-bin. However, the assumption in [25] is that the space target position and the corresponding bistatic angle are completely accurate. In practical systems, there are errors of the satellite position data obtained by the telemetry network. Those errors are accumulated with slow time when calculating the image distortion angle. Hence, little error of the target position affects the subsequent image distortion alleviation. Further consideration of the linear geometry alleviation method should be discussed for practical bistatic-ISAR systems.

In this paper, we focus on the alleviation of linear geometry distortions and propose a corresponding alleviation algorithm of space targets through exploiting prior information in the classical bistatic-ISAR system. First, we calculate the bistatic angles through exploiting prior information (the imaging geometry and orbital information of space targets). Second, we obtain the coefficients of first-order polynomial of bistatic angles using the least square error (LSE) method. Then, we construct compensation in terms of the linear spatial-variant terms and conduct restoration the process based on phase compensation along each range-bin. Finally, we obtain the well-restored image with real shape via the compression and rescaling of cross range.

This paper is organized as follows. The bistatic-ISAR theories are revisited and related distortions are analytically treated in Section 2. The linear geometry distortion alleviation algorithm is discussed in detail in Section 3. In Section 4, simulated results using both the ideal point scatterers dataset and the electromagnetic numerical dataset are presented, respectively. In Section 5, we draw the conclusions.

2. Signal Model with Distortions

The generic bistatic radar configuration is shown in Figure 1. The transmitting station and receiving station are separated. R_T and R_R denote the distances between the target and the transmitting station and receiving station, respectively. The length of baseline L is comparable with R_T and R_R . The bistatic angle formed by bistatic radar geometry is referred as β .

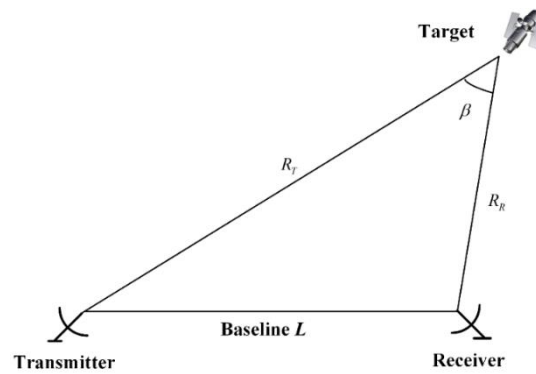


Figure 1. Generic bistatic radar configuration.

In the generic bistatic-ISAR system of the space target, assumptions of both the short CPI and far field are satisfied. The bistatic angle β_m at t_m and the distortion term $\cos \beta_m/2$ caused by the bistatic configuration can be represented as Equations (1) and (2) by first-order polynomial, respectively [6]:

$$\beta_m \approx \beta_0 + \Delta\beta t_m \tag{1}$$

where t_m is slow time, $\beta_0 = \beta(t_0)$ and $\Delta\beta = \left. \frac{d\beta(t_m)}{dt_m} \right|_{t_m=0}$.

$$\cos\left(\frac{\beta_m}{2}\right) \approx \cos\left(\frac{\beta_0}{2}\right) - \frac{\Delta\beta}{2} \sin\left(\frac{\beta_0}{2}\right) t_m = K_0 + K_1 t_m \tag{2}$$

where

$$K_0 = \cos\left(\frac{\beta_0}{2}\right) \quad K_1 = -\frac{\Delta\beta}{2} \sin\left(\frac{\beta_0}{2}\right) \tag{3}$$

The transmitted linear chirp modulation signal is as follows:

$$s_t(\hat{t}, t_m) = \text{rect}\left(\frac{\hat{t}}{T_p}\right) \exp\left[j2\pi\left(f_c t + \frac{1}{2}\mu\hat{t}^2\right)\right] \tag{4}$$

where pulse repetition period is T_{PRT} , the rectangle function is $\text{rect}(u) = \begin{cases} 1 & |u| \leq \frac{1}{2} \\ 0 & |u| > \frac{1}{2} \end{cases}$. $\hat{t} = t - t_m$ denotes fast time. T_p denotes pulse width. f_c denotes carrier frequency. μ denotes chirp rate.

If constraint of the range-bin migration is satisfied, after successful signal pre-processing and translational motion compensation, the phase change between each period caused by both translational motion and the propagation of electromagnetic wave e.g., refractive effect, is compensated. The signal of the n th range-bin is written as Equation (5). More details are available in [6].

$$s_n(t_m) = \sum_{i=1}^{L_n} A_i \exp\left(\frac{-j4\pi f_c}{c} \left(x_i \omega_0 t_m + y_i \left(1 - \frac{\omega_0^2 t_m^2}{2}\right)\right) (K_0 + K_1 t_m)\right) \tag{5}$$

where (x_i, y_i) are the coordinates of the i th scatterer, L_n is the scatterers number of the n th range-bin, A_i is the complex amplitude and ω_0 is the rotation velocity (RV).

The positions of range in Equation (5) are the same ($y_1 = y_2 = \dots = y_{L_n} = y_n$). Neglecting the constant and third-order terms, $s_n(t_m)$ can be rewritten as follows:

$$s_n(t_m) = \sum_{i=1}^{L_n} A_i \exp\left(\frac{-j2\pi f_c}{c} (2y_n K_1 t_m + 2\omega_0 x_i K_0 t_m + \gamma_i t_m^2)\right) \tag{6}$$

where $\gamma_i = 2\omega_0 x_i K_1 - y_n K_0 \omega_0^2$.

Apply Fourier transform (FT) to $s_n(t_m)$ in Equation (6) along the slow-time direction.

$$\begin{aligned}
 S_n(f_d) &= \int_0^T s_n(t_m) \exp(-j2\pi f_d t_m) dt_m \\
 &= \sum_{i=1}^{L_n} A_i psf_i \left(f_d - \left(f_i + \frac{2f_c K_1 y_n}{c} \right) \right)
 \end{aligned}
 \tag{7}$$

T denotes the CPI. f_d denotes the Doppler frequency. $f_i = 2f_c \omega_0 x_i K_0 / c$ is the Doppler frequency of i th scatterer. $psf_i(f_d) = T \sin c(f_d) \otimes D_i(f_d)$ is the point spread function of i th scatterer. Symbol \otimes denotes the convolution operator. $D_i(f_d)$ is the FT of the quadratic distortion terms of the i th scatterer.

$$D_i(f_d) = \int_0^T A_i \exp\left(\frac{-j2\pi f_c}{c} \gamma_i t_m^2\right) \exp(-j2\pi f_d t_m) dt_m
 \tag{8}$$

Because the quadratic distortion terms are relatively small in generic bistatic-ISAR systems [23], we focus on the linear distortion term. As expressed in Equation (7), scatterers cross-range positions are shifted by $2f_c K_1 y_n / c$ along the cross-range direction in the n th range-bin. The shift of Doppler depends on the range position y_n and leads to the sheared shape of bistatic-ISAR image.

3. Linear Geometry Distortion Alleviation Algorithm

3.1. Exploiting Prior Information

The configuration of bistatic-ISAR systems is shown in Figure 2. Tx and Rx represent the transmitting station and receiving station, respectively. The baseline length is referred to L . BEM radar is the instantaneous approximation of bistatic-ISAR system under certain constraints [6,14]. The target velocity is referred as V . O is the target’s mass center. The distances between O and the transmitting station and receiving station are R_{TO} and R_{RO} respectively. β_0 denotes initial bistatic angle at t_0 . ζ_0 denotes the initial view angle of the transmitting station at t_0 . We establish the coordinate system xOy according to the right hand rule. O is the origin of xOy . Bisector of β_0 is the y axis. (x_p, y_p) are the coordinates of the scatterer P in xOy . d denotes the length of OP . The target’s mass center O moves to O_m at t_m . And the new coordinate system $x'O_m y'$ is translational motion of the old coordinate system xOy . β_m denotes the bistatic angle of slow time t_m . ζ_m denotes the view angle of the transmitting station of slow time t_m . With the bisector of β_m as v axis and O_m as the origin, we establish the coordinate system $uO_m v$ according to the right hand rule. (x_{Pm}, y_{Pm}) are the coordinates of the scatterer P in the $uO_m v$. α_m is the angle between $O_m P_m$ and u axis. θ_m is the change of equivalent view angle of BEM radar. The distances between P_m and the transmitting station and receiving station are R_{TPm} and R_{RPm} respectively. The distances between O_m and the transmitting station and receiving station are R_{TOm} and R_{ROm} respectively.

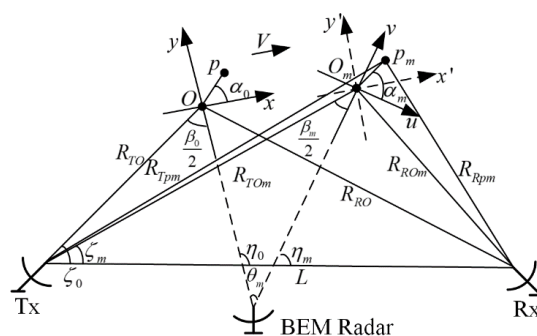


Figure 2. Imaging geometry of bistatic inverse synthetic aperture radar (bistatic-ISAR) system.

Two positions of the transmitting station and receiving station are known previously in the bistatic-ISAR system. Positions of the space targets can be calculated by combining the orbital motion model with precise ephemeris, as we mentioned in [10]. The precise ephemeris can be calculated from the telemetry data. Telemetry data can be achieved through fusing the radar and optical sensor results in telemetry network. R_{TOm} , R_{ROm} and L can be calculated according to the geometry shown in Figure 2. Thus, the time variant bistatic angle β_0 and β_m , the corresponding view angles ζ_0 and ζ_m can be obtained by the following equations:

$$\beta_0 = \arccos\left(\frac{R_{TO}^2 + R_{RO}^2 - L^2}{2R_{TO}R_{RO}}\right) \tag{9}$$

$$\beta_m = \arccos\left(\frac{R_{TOm}^2 + R_{ROm}^2 - L^2}{2R_{TOm}R_{ROm}}\right) \tag{10}$$

$$\zeta_0 = \arccos\left(\frac{R_{TO}^2 + L^2 - R_{RO}^2}{2R_{TO}L}\right) \tag{11}$$

$$\zeta_m = \arccos\left(\frac{R_{TOm}^2 + L^2 - R_{ROm}^2}{2R_{TOm}L}\right) \tag{12}$$

The corresponding η_0 and η_m can be obtained by

$$\eta_0 = \zeta_0 + \beta_0/2 \tag{13}$$

$$\eta_m = \zeta_m + \beta_m/2 \tag{14}$$

The change of equivalent view angle of BEM radar θ_m (the equivalent rotation angle $(\alpha_m - \alpha_0)$) is calculated by

$$\theta_m = \eta_0 - \eta_m \tag{15}$$

As mentioned, the bistatic angle can be approximated by Equation (1) [$\beta_m \approx \beta_0 + \Delta\beta t_m$]. Therefore, we can estimate the β_0 and $\Delta\beta$ as $\hat{\beta}_0$ and $\hat{\Delta\beta}$ using the LSE method based on β_m , respectively. Then, we estimate K_0 and K_1 through the following equations respectively:

$$\hat{K}_0 = \cos\left(\frac{\hat{\beta}_0}{2}\right) \tag{16}$$

$$\hat{K}_1 = -\frac{\hat{\Delta\beta}}{2} \sin\left(\frac{\hat{\beta}_0}{2}\right) \tag{17}$$

We obtain the estimated RV $\hat{\omega}_0$ by the CPI and θ_m . We should note \hat{K}_0 , \hat{K}_1 and $\hat{\omega}_0$ can be obtained with high accuracy. $\xi_{R_{TPm}}$ and $\xi_{R_{RPm}}$ (the errors of the distance R_{TPm} and R_{RPm}) are relatively small compared with R_{TPm} and R_{RPm} and L in the generic bistatic-ISAR system observing space targets. ξ_{β_m} (the relative error of β_m) and ξ_{θ_m} (the relative error of θ_m) are calculated according to the geometry shown in Figure 2. In this scenario, those two ξ_{β_m} and ξ_{θ_m} are relatively small, e.g., $\xi_{\beta_m} = 8.13 \times 10^{-6}$ and $\xi_{\theta_m} = 8.61 \times 10^{-6}$, when $\xi_{R_{TPm}} = 2$ m, $\xi_{R_{RPm}} = 2$ m, $R_{TPm} = 305.29$ km, $R_{RPm} = 603.45$ km, and $L = 800$ km. The LSE method can find the optimum fitting coefficients of given data set. For more details, see our previous discussion in [27].

3.2. Compensation of Linear Spatial-Variant Phase Terms

As mentioned, the first order term $\exp\left(\frac{-j4\pi f_c}{c} y_n K_1 t_m\right)$ of the phase term depends on y_n of the scatterers. It is the linear spatial-variant phase term. The range position y_n is written with respect of range-bin index:

$$y_n = (n - n_c)\rho_y \tag{18}$$

where n represents the range-bin index of y_n and n_c represents the unknown index of range-bin of equivalent RC. Length of a sampling point along the direction of range ρ_y can be written as [6]:

$$\rho_y = \frac{c}{2f_s \cos(\beta_0/2)} = \frac{c}{2f_s K_0} \tag{19}$$

where the f_s is the sampling rate.

By substituting Equation (18) into Equation (6), the signal of the n th range-bin $s_n(t_m)$ becomes

$$s_n(t_m) = \sum_{i=1}^{L_n} A_i \exp\left(\frac{-j2\pi f_c}{c} (2n\rho_y K_1 t_m - 2n_c \rho_y K_1 t_m + 2\omega_0 x_i K_0 t_m + \gamma_i t_m^2)\right) \tag{20}$$

According to Equation (20), the linear geometry distortion is related to the $f_c n \rho_y K_1 t_m / c$. We can estimate the coefficients K_0, K_1 and the ω_0 in advanced by exploiting prior information. Therefore, we can construct the spatial-variant compensation term φ_c in Equation (21) to alleviate the distortion.

$$\varphi_c = \exp\left(\frac{j4\pi f_c}{c} n \rho_y K_1 t_m\right) \tag{21}$$

Multiplying Equation (20) by Equation (21), the restoration of $s_n(t_m)$ can be written as

$$\bar{s}_n(t_m) = \sum_{i=1}^{L_n} A_i \exp\left(\frac{-j2\pi f_c}{c} (-2n_c \rho_y K_1 t_m + 2\omega_0 x_i K_0 t_m + \gamma_i t_m^2)\right) \tag{22}$$

The FT of the restored $\bar{s}_n(t_m)$ are obtained as follows

$$\bar{S}_n(f_d) = \sum_{i=1}^{L_n} A_i p_s f_i (f_d - f_i - f_{rc}) \tag{23}$$

where f_i represents the Doppler frequency of i th scatterer defined in Equation (7) and $f_{rc} = -2f_c K_1 n_c \rho_y / c$. f_{rc} only leads to corresponding amount of shift of the slow time compression data over all range-bins. In turn, the shape of the target does not change with the unknown index of the range-bin of equivalent RC n_c . It does not need to estimate n_c . Thus, the restored image with correct shape can be obtained by the spatial-variant compensation term φ_c in Equation (21).

3.3. Algorithm Summary

The overall algorithm of the linear geometry distortion alleviation is summarized.

Step 1: Perform pulse compression along range direction and translational motion compensation on the received bistatic-ISAR signal and obtain the one-dimensional range profile expressed in Equation (6).

Step 2: Calculate time variant bistatic angles β_m and change of the equivalent view angle of BEM radar θ_m (equivalent rotation angle), according to the geometry shown in Figure 2 and the positions of transmitting station, receiving station and space target (prior information).

Step 3: Estimate $\hat{\beta}_0$ and $\hat{\Delta\beta}$ based on β_m by the LSE method, respectively. Calculate RV $\hat{\omega}_0$ according to θ_m / CPI . Calculate \hat{K}_0 and \hat{K}_1 according to Equations (16) and (17), respectively.

Step 4: Construct phase terms for compensation according to Equation (21) and compensate the signal $s_n(t_m)$ of each range-bin with the corresponding compensation term.

Step 5: Apply FT to the restored data along slow-time direction and obtain the rescale the image with \hat{K}_0 and $\hat{\omega}_0$ to display the real shape of the target.

4. Results and Discussion

We conduct the simulations based on an ideal point scatterers dataset using a space target model and an electromagnetic scattering dataset using a typical satellite model.

4.1. Simulation Setting

The simulation scenario is selected as follows. The transmitting station and receiving station are located at Beijing and Shanghai respectively. The International Space Station orbit is chosen as the simulation orbit. The two-line elements (TLE) of the International Space Station are shown in Table 1.

Table 1. Two-line elements (TLE) of the International Space Station (12 September 2018).

1 25544U 98067A 18255.09915832 .00001088 00000-0 23933-4 0 9999
2 25544 51.6419 305.5808 0005084 148.3817 299.1230 15.53835622132031

The International Space Station orbit is determined by its TLE data (provided by the Space-Surveillance-Network of America). The epoch time in the initial orbital elements is on 12 September 2018 at 02:22:47. The visible time-window of the bistatic-ISAR system is from 14:28:15 to 14:37:09 on 12 September 2018. We chose the particular CPI with the bistatic angle linear change from the visible time window as the imaging segment.

The simulation scenario is illustrated in Figure 3.

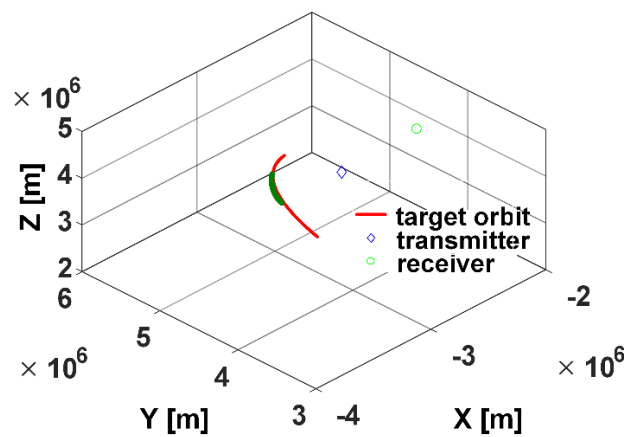


Figure 3. Simulation scenario.

The parameters of the bistatic-ISAR system are listed in Table 2.

Table 2. Parameters of the bistatic inverse synthetic aperture radar (bistatic-ISAR) system.

Parameter	Value	Parameter Name	Value
Carrier frequency	10 GHz	Sample frequency	800 MHz
Signal bandwidth	600 MHz	Pulse repetition frequency	100 Hz
Pulse width	20 us	Accumulated pulses	512
Integration angle	4.68°	Envelope alignment	Cross-correlation accumulation
Phase compensation	Phase gradient auto-focus	Image algorithm	Range Doppler
\hat{K}_0	0.7425	\hat{K}_1	-0.0073

4.2. Simulation Based on Two Datasets

The bistatic angles are calculated by the imaging geometry and the positions of the space target, transmitting station and receiving station. Figure 4 shows the change of bistatic angles with the pulse number within the CPI. Bistatic angles β_m within the CPI almost change linearly with slow time. That is because the imaging segment is chosen with the bistatic angle linear change. Figure 5 shows the change of θ_m with the pulse number within the CPI. The rotation angle also changes linearly with slow time. The variation of the rotation angle is 4.68° . The equivalent RV is 0.016 rad/s.

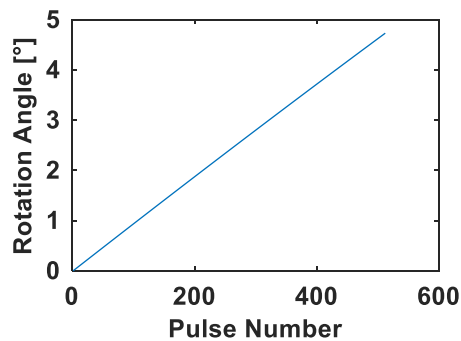


Figure 4. Bistatic angle β_m .

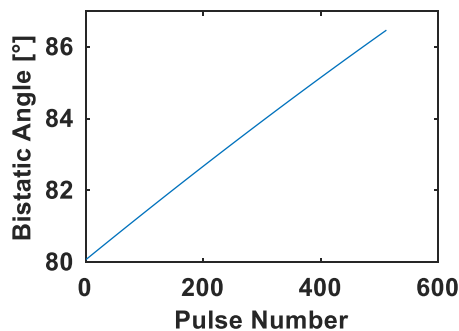


Figure 5. Equivalent rotation angle θ_m .

The ideal point scatterer dataset of the space target shown in Figure 6a is comprised of 307 point scatterers. For the ideal point scatterer, scattering coefficient of each scatterer is 1. The typical satellite shown in Figure 7a has x, y and z extends of 40.09 m, 30.37 m, and 20.74 m, respectively. The ISAR image is the electromagnetic reflection of targets in the RD domain. It is dependent on the instantaneous radar cross section (RCS) distribution on the imaging plane. For further assessment of the proposed algorithm, the bistatic electromagnetic RCS dataset of the typical satellite is obtained by the numerical physical optics technique. The echo data corresponding to the two datasets respectively are generated by the method we proposed in [8].

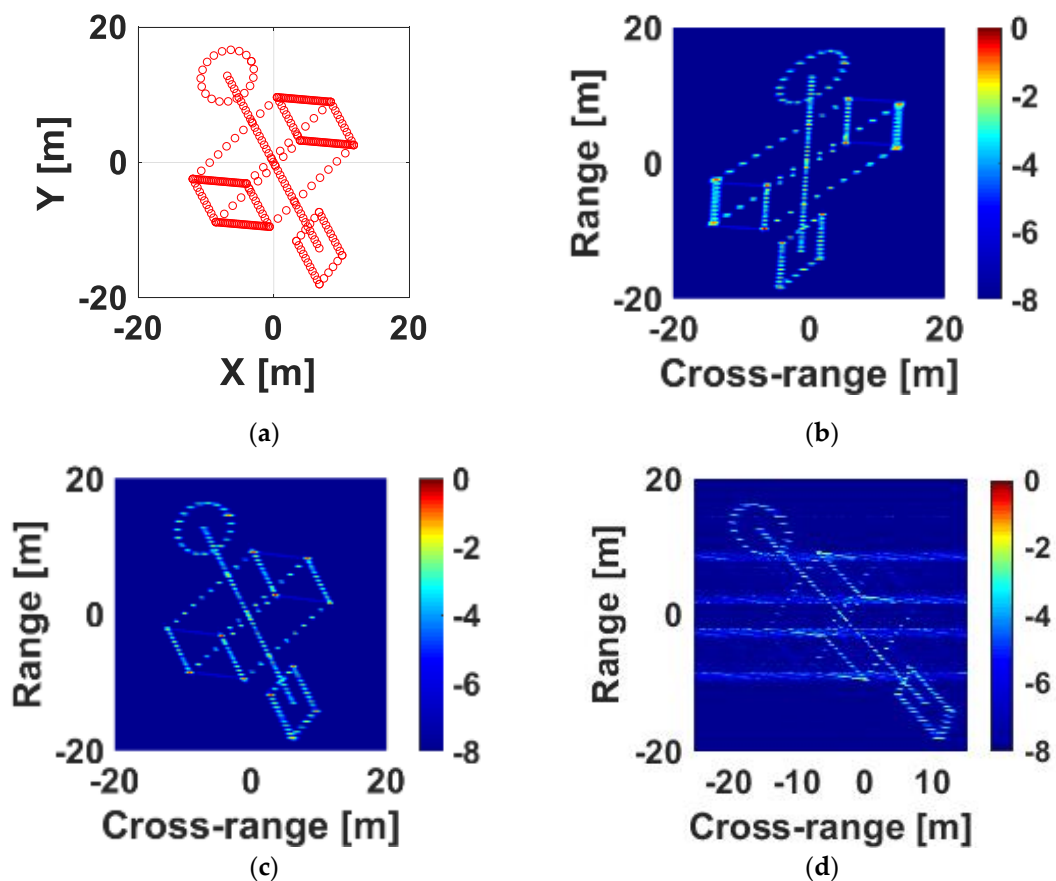


Figure 6. Results using the ideal point scatterers dataset: (a) The ideal point scatterers dataset (view of the line of sight (LOS) of bistatic equivalent monostatic (BEM) radar); (b) Before linear geometry distortion alleviation; (c) After linear geometry distortion alleviation with the proposed algorithm; (d) After linear geometry distortion alleviation with the algorithm in [25].

The envelope alignment and the auto-focusing are achieved by the maximum cross-correlation algorithm and phase gradient auto-focus (PGA) algorithm, respectively. Then, the images of Figures 6b and 7b are obtained by the RD imaging algorithm.

Due to the linear geometry distortion caused by time variant bistatic angles, the targets shape in Figures 6b and 7b are sheared. Using the proposed linear geometry distortion alleviation algorithm, the linear geometry distortions are alleviated in Figures 6c and 7c (compare Figure 6b with Figure 6c, compare Figure 7b with Figure 7c). The shape of the targets in the restored Figures 6c and 7c are consistent with the corresponding ones in Figures 6a and 7a (view of the LOS of BEM radar), respectively. It is beneficial to targets recognition.

The real shape of the target cannot be obtained by the algorithm in [25] and the image of several range-bins is defocused (Figures 6d and 7d). The reason is that the assumption of complete accurate prior information is not satisfied in practical system and the image distortion angle is sensitive to the errors of prior information. Meanwhile, the results of the electromagnetic numerical dataset of typical satellite in Figure 7 and the comparison between proposed algorithm and the algorithm in [25] further verified the robustness of the presented algorithm.

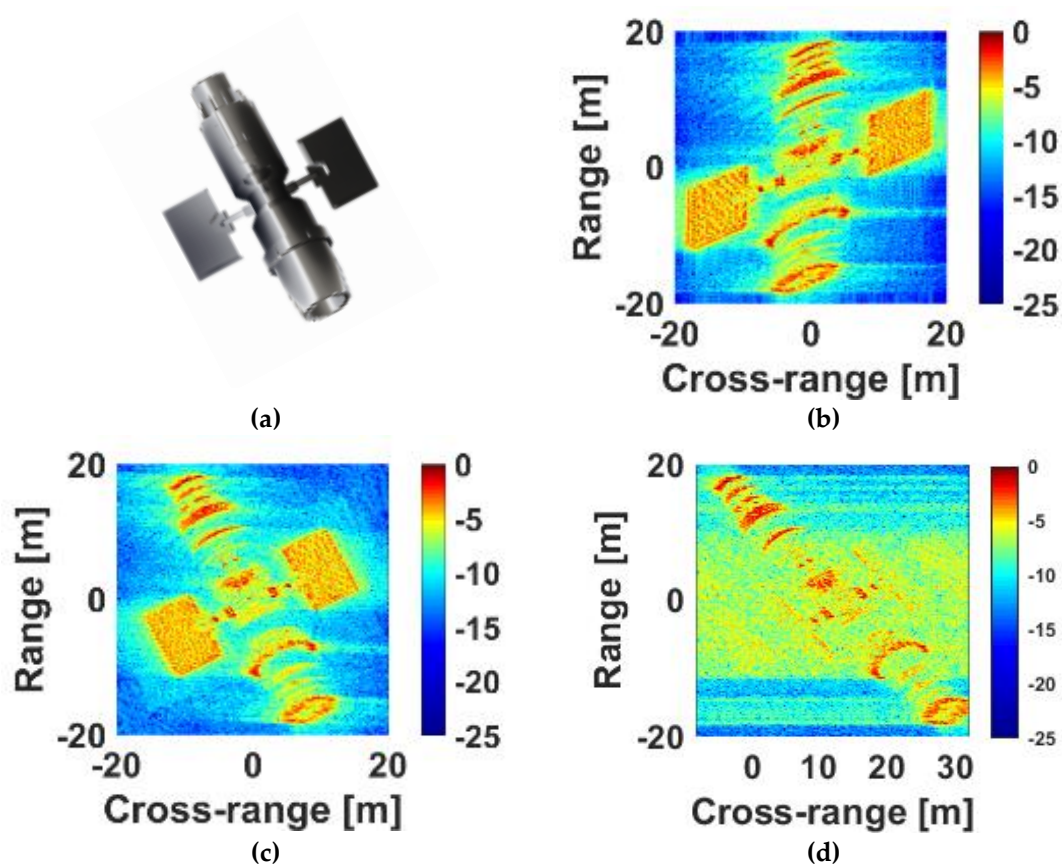


Figure 7. Results using the electromagnetic numerical radar cross section (RCS) dataset: (a) Computer aided design model of the satellite (the view of LOS of BEM radar); (b) Before linear geometry distortion alleviation; (c) After linear geometry distortion alleviation with the proposed algorithm; (d) After linear geometry distortion alleviation with the algorithm in [25].

5. Conclusions

We present a clear procedure of the linear geometry distortion alleviation algorithm based on prior information for better utilization of the bistatic-ISAR image. Simulated results of both ideal point scatterer dataset of space target model and electromagnetic numerical dataset of the typical satellite model verify the feasibility and robustness of proposed algorithm. The comparisons of the results before and after the alleviation indicate that our algorithm is capable of restoring the linear geometry distortion and providing the real shape of the target. The restored results are beneficial to further target classification and recognition.

Author Contributions: Conceptualization, L.S. and C.S.; methodology, L.S., B.G. and N.H.; software, J.M.; validation, L.S. and X.Z.; formal analysis, L.S. and X.Z.; investigation, B.G. and N.H.; resources, J.M.; data curation, L.S. and B.G.; writing—original draft preparation, L.S.; writing—review and editing, B.G. and N.H.; supervision, C.S.; funding acquisition, C.S.

Funding: The research was funded by the National Natural Science Foundation of China under Grant 61601496 and 61701544.

Acknowledgments: We appreciate the editors and peer reviewers for their valuable comments and suggestions.

Conflicts of Interest: The authors declare no conflicts of interest.

References

- Walker, J.L. Range-doppler imaging of rotating objects. *IEEE Trans. Aerosp. Electron. Syst.* **1980**, *16*, 23–52. [[CrossRef](#)]

2. Xing, M.; Wu, R.; Li, Y.; Bao, Z. New ISAR imaging algorithm based on modified Wigner-Ville distribution. *IET Radar Sonar Navig.* **2008**, *3*, 70–80. [[CrossRef](#)]
3. Zhao, J.; Zhang, M.; Wang, X.; Cai, Z.; Nie, D. Three-dimensional super resolution ISAR imaging based on 2D unitary ESPRIT scattering centre extraction technique. *IET Radar Sonar Navig.* **2017**, *11*, 98–106. [[CrossRef](#)]
4. Lv, Y.; Wu, Y.; Wang, H.; Qiu, L.; Jiang, J.; Sun, Y. An Inverse Synthetic Aperture Ladar Imaging Algorithm of Maneuvering Target Based on Integral Cubic Phase Function-Fractional Fourier Transform. *Electronics* **2018**, *7*, 148. [[CrossRef](#)]
5. Giusti, E.; Martorella, M.; Capria, A. Polarimetrically-Persistent-Scatterer-Based Automatic Target Recognition. *IEEE Trans. Geosci. Remote Sens.* **2011**, *49*, 4588–4599. [[CrossRef](#)]
6. Martorella, M.; Palmer, J.; Homer, J.; Littleton, B.; Longstaff, D. On bistatic inverse synthetic aperture radar. *IEEE Trans. Aerosp. Electron. Syst.* **2007**, *43*, 1125–1134. [[CrossRef](#)]
7. Bai, X.; Zhou, F.; Xing, M.; Bao, Z. Scaling the 3-D Image of Spinning Space Debris via Bistatic Inverse Synthetic Aperture Radar. *IEEE Geosci. Remote Sens. Lett.* **2010**, *7*, 430–434. [[CrossRef](#)]
8. Guo, B.F.; Shang, C.X.; Wang, J.L. Bistatic ISAR echo simulation of space target based on two-body model. *Syst. Eng. Electron.* **2016**, *38*, 1771–1779. [[CrossRef](#)]
9. Ma, J.; Gao, M.; Hu, W.; Di, X.; Shi, L. Optimum Distribution of Multiple Location ISAR and Multi-angles Fusion Imaging for Space Target. *J. Electron. Inf. Technol.* **2017**, *39*, 2834–2843. [[CrossRef](#)]
10. Ma, J.T.; Gao, M.G.; Guo, B.F.; Dong, J.; Xiong, D.; Feng, Q. High resolution inverse synthetic aperture radar imaging of three-axis-stabilized space target by exploiting orbital and sparse priors. *Chin. Phys. B* **2017**, *26*, 108401. [[CrossRef](#)]
11. Tian, B.; Zou, J.; Xu, S.; Chen, Z. Squint model interferometric ISAR imaging based on respective reference range selection and squint iteration improvement. *IET Radar Sonar Navig.* **2015**, *9*, 1366–1375. [[CrossRef](#)]
12. Han, N.; Li, B.; Wang, L.; Tong, J.; Guo, B. Algorithm for autofocusing of bistatic ISAR of space target based on sparse decomposition. *Acta Aeronaut. Astronaut. Sin.* **2018**, *39*, 322037. [[CrossRef](#)]
13. Martorella, M. Analysis of the Robustness of Bistatic Inverse Synthetic Aperture Radar in the Presence of Phase Synchronisation Errors. *IEEE Trans. Aerosp. Electron. Syst.* **2011**, *47*, 2673–2689. [[CrossRef](#)]
14. Martorella, M.; Cataldo, D.; Brisken, S. Bistatically equivalent monostatic approximation for bistatic ISAR. In Proceedings of the IEEE Radar Conference, Ottawa, ON, Canada, 29 April–3 May 2013; pp. 1–5.
15. Shi, L.; Guo, B.F.; Ma, J.T.; Shang, C.X.; Zeng, H.Y. A Novel Channel Calibration Method for Bistatic ISAR Imaging System. *Appl. Sci.* **2018**, *8*, 2160. [[CrossRef](#)]
16. Sun, S.B.; Jiang, Y.C.; Yuan, Y.S.; Hu, B.; Yeo, T.S. Defocusing and distortion elimination for shipborne bistatic ISAR. *Remote Sens. Lett.* **2016**, *7*, 523–532. [[CrossRef](#)]
17. Xiong, D.; Zhang, X.; Wang, J.; Zhao, H.; Gao, M. Reception and calibration of bistatic SF ISAR imaging system with wideband receiver. *IET Radar Sonar Navig.* **2017**, *11*, 379–385. [[CrossRef](#)]
18. Zhang, S.S.; Sun, S.B.; Zhang, W.; Zong, Z.L.; Yeo, T.S. High-Resolution Bistatic ISAR Image Formation for High-Speed and Complex-Motion Targets. *IEEE J. Sel. Top. Appl. Earth Obs. Remote Sens.* **2015**, *8*, 3520–3531. [[CrossRef](#)]
19. Zhao, L.; Gao, M.; Martorella, M.; Stagliano, D. Bistatic three-dimensional interferometric ISAR image reconstruction. *IEEE Trans. Aerosp. Electron. Syst.* **2015**, *51*, 951–961. [[CrossRef](#)]
20. Chen, S.; Zhao, H.C.; Zhang, S.N.; Chen, Y. An improved back projection imaging algorithm for dechirped missile-borne SAR. *Acta Phys. Sin.* **2014**, *62*, 218405. [[CrossRef](#)]
21. Horvath, M.S.; Gorham, L.A.; Rigling, B.D. Scene Size Bounds for PFA Imaging with Postfiltering. *IEEE Trans. Aerosp. Electron. Syst.* **2013**, *49*, 1402–1406. [[CrossRef](#)]
22. Cataldo, D.; Martorella, M. Bistatic ISAR Distortion Mitigation via Superresolution. *IEEE Trans. Aerosp. Electron. Syst.* **2018**, *54*, 2143–2157. [[CrossRef](#)]
23. Jiang, Y.; Sun, S.; Yeo, T.S.; Yuan, Y. Bistatic ISAR distortion and defocusing analysis. *IEEE Trans. Aerosp. Electron. Syst.* **2016**, *52*, 1168–1182. [[CrossRef](#)]
24. Ma, C.Z.; Yeo, T.S.; Guo, Q.; Wei, P.J. Bistatic ISAR Imaging Incorporating Interferometric 3-D Imaging Technique. *IEEE Trans. Geosci. Remote Sens.* **2012**, *50*, 3859–3867. [[CrossRef](#)]
25. Guo, B.F.; Shang, C.X.; Wang, J.L.; Gao, M.G.; Fu, X.J. Correction of migration through resolution cell in bistatic inverse synthetic aperture radar in the presence of time variant bistatic angle. *Acta Phys. Sin.* **2014**, *63*, 238406.

26. Dong, J.; Gao, M.G.; Shang, C.X.; Fu, X.J. The Image Plane Analysis and Echo Model Amendment of Bistatic ISAR. *J. Electron. Inf. Technol.* **2010**, *32*, 1855–1862. [[CrossRef](#)]
27. Zhu, X.X.; Hu, W.H.; Ma, J.T.; Guo, B.F.; Xue, D.F. ISAR autofocusing imaging with sparse apertures and time variant bistatic angle. *Acta Aeronaut. Astronaut. Sin.* **2018**, *39*, 322059. [[CrossRef](#)]



© 2019 by the authors. Licensee MDPI, Basel, Switzerland. This article is an open access article distributed under the terms and conditions of the Creative Commons Attribution (CC BY) license (<http://creativecommons.org/licenses/by/4.0/>).